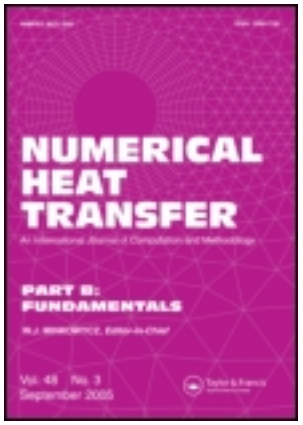


Numerical Heat Transfer, Part B: Fundamentals: An International Journal of Computation and Methodology
Publication details, including instructions for authors and subscription information:
http://www.tandfonline.com/loi/unhb20

# A Pressure-Correction Method for Incompressible Flows Using Unstructured Meshes

Yeng-Yung Tsui [a] & Yeng-Feng Pan [a]
[a] Department of Mechanical Engineering , National Chiao Tung University , Hsinchu, Taiwan, Republic of China
Published online: 24 Feb 2007.

To cite this article: Yeng-Yung Tsui & Yeng-Feng Pan (2006) A Pressure-Correction Method for Incompressible Flows Using Unstructured Meshes, Numerical Heat Transfer, Part B: Fundamentals: An International Journal of Computation and Methodology, 49:1, 43-65

To link to this article: http://dx.doi.org/10.1080/10407790500344084

*Numerical Heat Transfer, Part B*, 49: 43–65, 2006

ISSN: 1040-7790 print/1521-0626 online
DOI: 10.1080/10407790500344084

Taylor & Francis
Taylor & Francis Group

# A PRESSURE-CORRECTION METHOD FOR INCOMPRESSIBLE FLOWS USING UNSTRUCTURED MESHES

**Yeng-Yung Tsui and Yeng-Feng Pan**
*Department of Mechanical Engineering, National Chiao Tung University, Hsinchu, Taiwan, Republic of China*

***A pressure-correction method is presented to solve incompressible viscous flows. The development of this method is aimed at dealing with unstructured grids, which are made of control volumes with arbitrary topology. To enhance the robustness of the method, all variables are collocated on the cell centers. The divergence theorem of Gauss is employed for discretization, and vector forms are used throughout the formulation. In this way the method is equally applicable to two- and three-dimensional problems. An overrelaxed approach is adopted for the approximation of the cross-diffusion flux to deal with "skew" grids. It can be seen that this approach is equivalent to some other approximations available in the literature. However, the present approach is more suitable for three-dimensional calculations without causing complication. This overrelaxed approach is also employed in the pressure-correction equation derived from the continuity constraint. Most prevailing methods simply ignore the cross-derivative term of the pressure-correction equation, which not only causes instability but also slows down convergence rate if the grid is skew. This cross-derivative term is taken into account in the present calculations by using a successive correction procedure. The application of the methodology to flows in lid-driven cavities and diffusers shows that no more than two pressure-correction steps are enough to obtain fast and stable convergence. The method is also applied to a three-dimensional flow in an impeller-stirred tank.***



## INTRODUCTION

The development of computational fluid dynamics has reached such a mature stage that viscous flow, either laminar or turbulent, can be analyzed by solving the full Navier-Stokes equations in an extremely complex geometry. In handling irregular boundaries, finite-element methods have been preferred to other methods such as finite-difference schemes because they can use unstructured, triangular meshes which can easily be generated to cope with arbitrary geometry. However, the recent development of finite-volume methods is drawing much attention due to the following reasons. First, the finite-volume methods satisfy the physical principle of conservation law by using the Gauss's divergence theorem as basis. Second, they are

Received 7 September 2004; accepted 17 August 2005.

The work was supported by the Science Research Council of the Republic of China under the contracts NSC 91-2212-E-009-051 and NSC 93-2212-E-009-012.

Address correspondence to Yeng-Yung Tsui, Department of Mechanical Engineering, National Chiao Tung University, Hsinchu 300, Taiwan, Republic of China. E-mail: yytsui@mail.nctu.edu.tw

## NOMENCLATURE

| | |
|---|---|
| $A_C$, $A_P$ | coefficients of the difference equation |
| $A_C^P$ | coefficient of the pressure difference equation |
| $\vec{d}$ | a vector in the direction of $\vec{\delta}_{PE}$ |
| $D$ | pressure coefficient in the difference equation |
| $\vec{e}_d$ | unit vector in the direction of $\vec{\delta}_{PE}$ |
| $\vec{e}_s$ | unit surface vector |
| $\vec{e}_t$ | unit vector parallel to the cell face |
| $f_p$ | spatial weighting factor |
| $F$ | flux |
| $\dot{m}$ | mass flux |
| $p$ | pressure |
| $p'$ | pressure correction |
| $\vec{r}_e$ | distance vector from the upstream cell node to the face node |
| $s$ | magnitude of $\vec{s}$ |
| $\vec{s}$ | surface vector of the cell face |
| $S$ | source term of the difference equation |
| $S_{p1}$, $S_{p2}$ | source terms of the pressure difference equation |
| $S_\phi$ | source term of the transport equation |
| $\vec{V}$ | flow velocity vector |
| $\gamma$ | blending factor |
| $\Gamma$ | diffusion coefficient |
| $\vec{\delta}_{PE}$ | distance vector from node $P$ to node $E$ |
| $\theta$ | angle between the surface vector and $\vec{\delta}_{PE}$ |
| $\rho$ | density |
| $\phi$ | an entity |

**Subscripts**

| | |
|---|---|
| $C$ | neighboring cell nodes |
| $e$ | east face node |
| $E$ | east cell node |
| $f$ | a face node |
| $P$ | primary cell node |

**Superscripts**

| | |
|---|---|
| $c$ | convection |
| $d$ | diffusion |
| $HD$ | high-order scheme |
| $UD$ | upwind scheme |
| (1) | first correction |
| (2) | second correction |

relatively easy to implement and the difference equations raised can be solved efficiently using iterative methods because the generated coefficient matrices inherit the sparse character of the finite-difference methods. Third, they allow the use of mixed grids consisting of cells with various shapes without causing complication in formulation.

In solving incompressible flow or low-Mach-number flow, pressure-based methods are most widely used, since the velocity is mainly driven by pressure force. In these methods a pressure equation or a pressure-correction equation is derived by forcing the velocity field to satisfy the continuity constraint. The momentum equation and the pressure equation, or the pressure-correction equation, are solved for velocity and pressure in a segregated manner. An important issue which affects the coupling between the velocity and the pressure is the placement of the velocity and the pressure on the grid. A sketch of some grid layouts in two dimensions is given in Figure 1. It has been long recognized that the collocation of pressure and velocity [1–6], such as the one shown in Figure 1*a*, would cause pressure wiggles since the two variables are linked in a checkerboard manner. One way to circumvent this problem is to introduce artificial pressure dissipation explicitly [1]. The amount of dissipation is controlled via a damping coefficient. Partly due to the setting of the damping coefficient being case dependent, this method did not gain popularity. An effective way to conquer the oscillation is the use of staggered grids in which the pressure is placed at cell centroids while the velocity components are sited on the midpoints of cell faces, as shown in Figure 1*b* [7, 8]. In this manner the mass

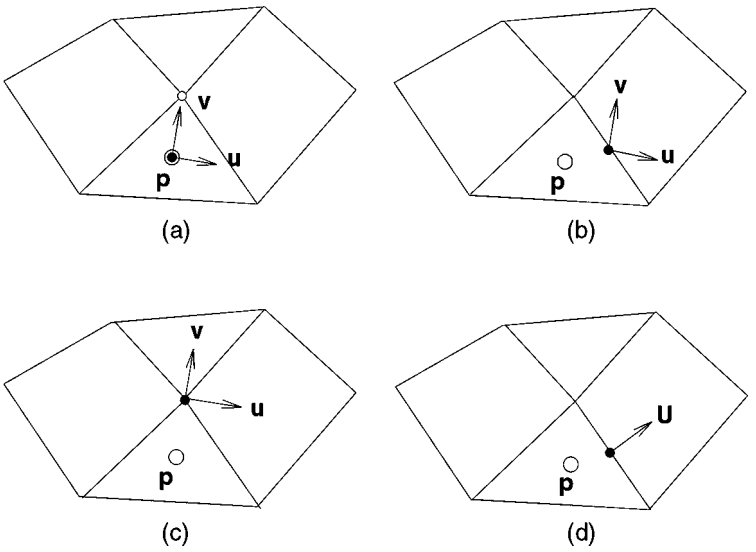


**Figure 1.** Variable grid arrangements.



fluxes crossing the cell faces, as required for the mass conservation for the pressure cells, are directly available. However, this arrangement becomes inefficient when the number of faces per cell increases. As an example, for a two-dimensional problem with the use of quadrilateral cells one must solve four momentum equations on two faces for each cell. Another drawback is that if the grid is "orthogonal" and the flow velocity is in the direction of a cell face, the velocity is not directly related to the pressures on the two cells sharing the face. In Figure 1*c* the velocity components are placed on cell vertices [9, 10]. It is obvious that the link between the velocity components and the pressure is weak. Thus, a special treatment is usually necessitated. The placement of the velocity node in Figure 1*d* is the same as that in Figure 1*b*, i.e., on the cell faces. In the latter the Cartesian velocity components are the primary variables, whereas in the former it is the velocity component normal to the face being solved for [11–13]. The equation governing the normal velocity component is available by projecting the momentum equation onto the direction normal to the face. The tangential velocity component is obtained through a special interpolation procedure from the normal velocities on neighboring faces. The disadvantage of this method is the necessity for the edges of the primary grid and those of the dual grid for the velocity to be perpendicular to each other. If these two families of grids are not mutually orthogonal, the accuracy of the solution is severely damaged.

In view of the above discussion, the use of staggered grids is not without problems. Moreover, due to the displacement of the velocity from the pressure, another family of control volumes (complementary control volumes) needs to be constructed. As a result, formulations as well as programming become more complicated, especially for three-dimensional flow. In this work a method incorporating unstructured grids along with a pressure-correction equation is developed to solve

incompressible flows. The solution variables are collocated at cell centers (Figure 1a). To avoid the problem of velocity–pressure decoupling, the momentum interpolation method [14] is employed to calculate the mass fluxes across cell faces. It has been shown that this interpolation practice could lead to implicit fourth-order dissipation in pressure [15], which can effectively eliminate pressure oscillations. This unstructured-grid method possesses two important features. First, it is equally applicable to two- and three-dimensional problems without needing any modification or reformulation. Second, the geometric shape of the cell can be arbitrary, i.e., the number of surfaces for each cell can be variable. This feature is important for local grid refinement.



## NUMERICAL METHOD

The method described in the following can be equally applicable to both two- and three-dimensional flows. However, for the sake of easy presentation, only two-dimensional cases are considered.

The transport equation for an entity $\phi$ can be written in the following form:

$$\nabla \cdot (\rho \vec{V} \phi) = \nabla \cdot (\Gamma \nabla \phi) + S_\phi \tag{1}$$

where $S_\phi$ denotes the source term including the pressure gradient for the momentum equation. In the equation, the convection and diffusion terms are cast in the divergence form. In the finite-volume method the difference equation is obtained by first integrating over a control volume. Then, by using the Gauss's divergence theorem, the volume integral of convection and diffusion becomes a surface integral.

$$\int_s (\rho \vec{V} \phi) \cdot d\vec{s} = \int_s (\Gamma \nabla \phi) \cdot d\vec{s} + \int_{\Delta v} S_\phi \, dv \tag{2}$$

The control volume, in general, can be a polygon with arbitrary number of faces. For illustration, a two-dimensional control volume is presented in Figure 2*a*. The calculation of the convection and diffusion fluxes through the surface of the control volume can be approximated as

$$\int_s (\rho \vec{V} \phi) \cdot d\vec{s} = \sum_{f=1}^{n} F_f^c = \sum_{f=1}^{n} (\rho \vec{V} \cdot \vec{s})_f \phi_f \tag{3a}$$

$$\int_s (\Gamma \nabla \phi) \cdot d\vec{s} = \sum_{f=1}^{n} F_f^d = \sum_{f=1}^{n} (\Gamma \nabla \phi \cdot \vec{s})_f \tag{3b}$$

where $F_f^c$ and $F_f^d$, as defined in the equation, stand for the convection and diffusion fluxes through a face $f$, respectively, and $\vec{s}_f$ is the surface vector, which is always directed outwardly normal to the face of the control volume considered.

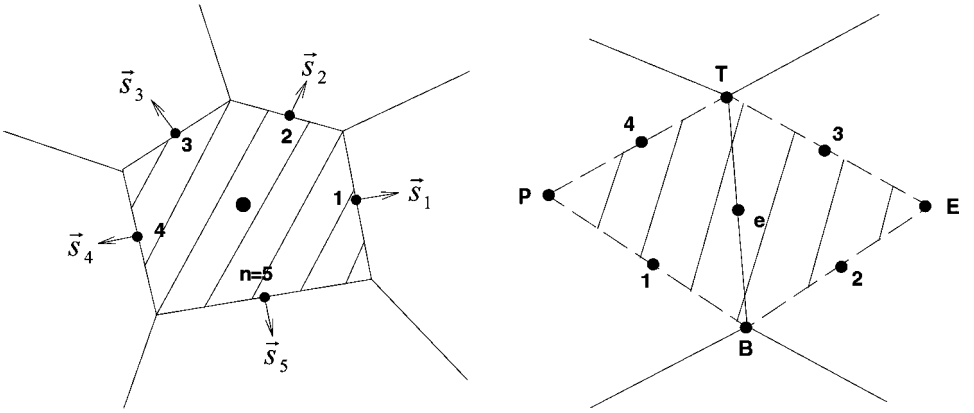


**Figure 2.** Illustration of (*a*) a typical control volume with arbitrary geometry and (*b*) a control volume surrounding face *e* for calculation of diffusion flux.



## Convection Fluxes

In evaluating the convection face flux $F_f^c$, both the mass flux and the entity at the face $\phi_f$ need to be approximated. The calculation of mass flux requires a special treatment and will be dealt with later. The approximation of $\phi_f$ is crucial to numerical accuracy and iteration stability. In the past decades a number of high-order difference schemes other than first-order upwind differencing and the central differencing were developed for structured grids. As examples, the QUICK scheme [16] and the linear upwind scheme [17] are the most popular among others. However, these high-order schemes require more than two nodes in the upstream direction for the face value approximation. Unlike the structured grid, in general, there is no certain grid direction in the unstructured grid system. In addition, the use of more than two nodes on one side of the face considered would significantly increase programming complication. Therefore, direct use of the above-mentioned high-order schemes is not suitable in unstructured grid calculations. In the computations of the present study the central differencing and an upwind-biased second-order scheme are employed. For a face *e*, the convection flux is arranged in the following form:

$$F_e^c = F_e^{UD} + \gamma(F_e^{HD} - F_e^{UD}) \tag{4}$$

where the superscripts *UD* and *HD* denote the upwind and the high-order schemes, respectively. The upwind-biased scheme is given by

$$\phi_e^{HD} = \phi_e^{UD} + \nabla\phi^{UD} \cdot \vec{r}_e \tag{5}$$

where the first term on the right-hand side simply represents the upwind difference approximation, $\nabla\phi^{UD}$ is the gradient of $\phi$ at the cell node upstream of the *e* face,

and $\vec{r}_e$ denotes the distance vector directed from the upstream cell node to the face node. Substituting this into Eq. (4) leads to

$$F_e^c = \dot{m}_e(\phi_e^{UD} + \gamma \nabla \phi^{UD} \cdot \vec{r}_e) \tag{6}$$

In the above, $\gamma$ is a value between 0 and 1. It plays the role of blending the high-order scheme and the upwind scheme. During calculation the upwind flux is treated implicitly to construct the coefficients of the difference equation. Thus, diagonal dominance is ensured for the coefficient matrix, which is beneficial to solution iteration. The rest of the flux is implemented explicitly and updated after each solution iteration.



### Diffusion Fluxes

A usual way to discretize the partial derivative of the diffusion flux is the use of Green's theorem or Gauss's theorem. For a control volume (*P-B-E-T*) surrounding the face point *e* shown in Figure 2*b*, this can be approximated as

$$\frac{\partial \phi}{\partial x} = \frac{1}{\Delta A} \oint \phi \, dy = \frac{1}{\Delta A} \sum_{j=1}^{4} \phi_j \, \Delta y_j \tag{7a}$$

$$\frac{\partial \phi}{\partial y} = -\frac{1}{\Delta A} \oint \phi \, dx = -\frac{1}{\Delta A} \sum_{j=1}^{4} \phi_j \, \Delta x_j \tag{7b}$$

where, for example,

$$\phi_1 = \frac{1}{2}(\phi_P + \phi_B) \tag{8a}$$

$$\Delta y_1 = y_B - y_P \tag{8b}$$

and $\Delta A$ is the area of the control volume *P-B-E-T*. The summation is over the four edges of the control volume. The above method is rather laborious because a lot of manipulation is required to yield the final form of the difference equation and the formulation is very complicated for three-dimensional problems.

To suit the need for comprehensive applications, a method was proposed by Jasak [18]. As given in Figure 3*a*, let $\vec{\delta}_{PE}$ be the vector connecting the cell nodes *P* and *E*, $\vec{s}$ the surface vector of the face, and $\vec{d}$ a vector in the direction of $\vec{\delta}_{PE}$. Then,

$$F_e^d = (\Gamma \nabla \phi \cdot \vec{s})_e = \Gamma_e \nabla \phi_e \cdot \vec{d} + \Gamma_e \nabla \phi_e \cdot (\vec{s} - \vec{d}) \tag{9}$$

A simple choice of $\vec{d}$, termed orthogonal-correction approach [18], is

$$\vec{d} = s \, \vec{e}_d = \frac{s}{\delta_{PE}} \vec{\delta}_{PE} \tag{10}$$

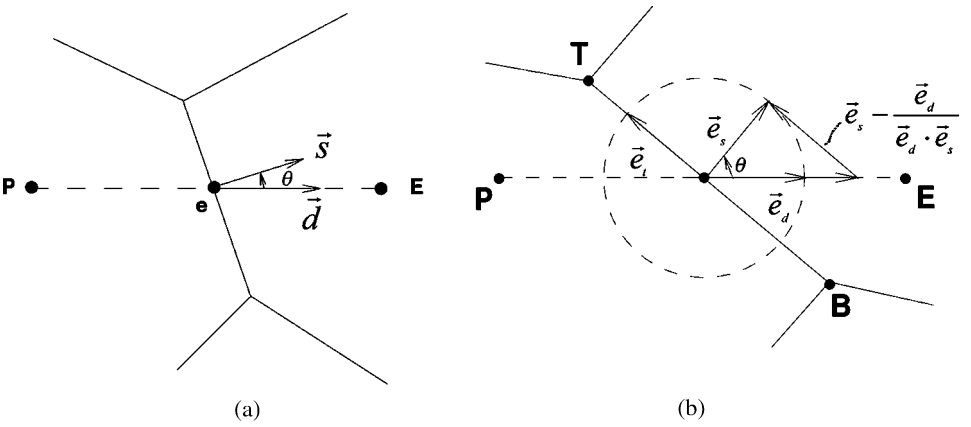


(a) (b)

**Figure 3.** Illustration of (*a*) vectors $\vec{d}$ and $\vec{s}$ and (*b*) the vector $\vec{s} - \vec{d}$ for the overrelaxed approach.

where $\vec{e}_d$ denotes the unit vector in the direction of $\vec{\delta}_{PE}$. Another choice, called overrelaxed approach [18], is given by

$$\vec{d} = \frac{s}{\vec{e}_d \cdot \vec{e}_s}\vec{e}_d = \frac{s^2}{\vec{\delta}_{PE} \cdot \vec{s}}\vec{\delta}_{PE} \tag{11}$$

where $\vec{e}_s$ denotes the unit vector normal to the face. It can be found that the two approaches become identical and equal to $\vec{s}$ when $\vec{\delta}_{PE}$ is in the same direction as $\vec{s}$. Unlike the orthogonal-correction approach, the magnitude of the overrelaxed approach varies with the skew angle θ between $\vec{s}$ and $\vec{\delta}_{PE}$. By introducing the overrelaxed approach into the first term of Eq. (9), the flux can be expressed as

$$F_e^d = \frac{\Gamma_e s^2}{\vec{\delta}_{PE} \cdot \vec{s}}(\phi_E - \phi_P) + \Gamma_e \overline{\nabla\phi}_e \cdot (\vec{s} - \vec{d}) \tag{12}$$

The gradient at the face in the second term is obtained via interpolation from the adjacent nodal values.

$$\overline{\nabla\phi}_e = (1 - f_P)\nabla\phi_P + f_P\nabla\phi_E \tag{13}$$

This term arises when the mesh is skew and disappears in orthogonal meshes. As in the above section, the deferred correction method is employed again in the solution iteration, that is, the first term is treated implicitly and the second term explicitly. The merit of using the overrelaxed approach and the deferred correction is that the coefficient of the implicit term increases with the skew angle θ, as long as $\vec{\delta}_{PE}$ is nonorthogonal to the face. Thus, the diagonal dominance of the coefficient matrix of the difference equation is enhanced.

In Eq. (12) the first term designates the normal diffusion and the second term the cross diffusion. The later is equivalent to the cross-derivative of the diffusion in

curvilinear structured grids. It can be shown in Figure 3*b* that

$$\vec{s} - \vec{d} = s\left(\vec{e}_s - \frac{\vec{e}_d}{\vec{e}_d \cdot \vec{e}_s}\right) = s \tan\theta \, \vec{e}_t \tag{14}$$

where $\theta$ is the skew angle between $\vec{e}_d$ and $\vec{e}_s$, and $\vec{e}_t$ is the unit vector parallel to the surface. Thus, for a two-dimensional problem the diffusion flux can be approximated by

$$F_e^d = \frac{\Gamma_e s^2}{\vec{\delta}_{PE} \cdot \vec{s}}(\phi_E - \phi_P) + \Gamma_e \tan\theta(\phi_T - \phi_B) \tag{15}$$

where the subscripts $T$ and $B$ denote the two cell vertices at the ends of the edge face, as shown in Figure 3*b*. If Eq. (15) is used in calculations, the vertex values must be approximated using cell values surrounding the vertices. This indicates that the computational molecule includes not only the neighboring cells sharing the faces with the control volume considered, but also the corner cells sharing the cell vertices.

There are a number of formulations for the diffusion flux, obtained in different ways. For the face control volume shown in Figure 4*a*, by using the approximations given in Eq. (7) for the gradient $\nabla\phi$, the following expression is obtained:

$$F_e^d = \frac{\Gamma_e s^2}{\left|\vec{\delta}_{PE} \times \vec{\delta}_{BT}\right|}(\phi_E - \phi_P) + \Gamma_e \frac{\vec{\delta}_{PE} \cdot \vec{\delta}_{BT}}{\left|\vec{\delta}_{PE} \times \vec{\delta}_{BT}\right|}(\phi_T - \phi_B) \tag{16}$$

This formulation can also be derived when considering the parallelogram control volume shown in Figure 4*b* used by Davidson [2].

Figure 4*a* shows two coordinates $\xi$ and $\eta$ which are in the directions of $\vec{\delta}_{PE}$ and $\vec{\delta}_{BT}$, respectively. By using these local curvilinear coordinates for $\nabla\phi \cdot \vec{s}$, a different expression for the diffusion flux is yielded [4–8]:

$$F_e^d = \frac{\Gamma_e s^2}{\vec{\delta}_{PE} \cdot \vec{s}}(\phi_E - \phi_P) + \Gamma_e \frac{\vec{\delta}_{PE} \cdot \vec{\delta}_{BT}}{\vec{\delta}_{PE} \cdot \vec{s}}(\phi_T - \phi_B) \tag{17}$$

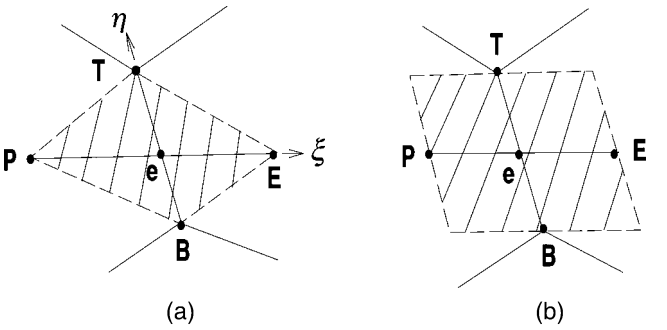


**Figure 4.** Illustration of two control volumes used for calculation of diffusion flux.

It is interesting to notice that the above two expressions (16) and (17) are exactly the same as Eq. (15) because

$$\left|\vec{\delta}_{PE} \times \vec{\delta}_{BT}\right| = \vec{\delta}_{PE} \cdot \vec{s} \tag{18a}$$

$$\frac{\vec{\delta}_{PE} \cdot \vec{\delta}_{BT}}{\left|\vec{\delta}_{PE} \times \vec{\delta}_{BT}\right|} = \frac{-\sin\theta}{\cos\theta} = -\tan\theta \tag{18b}$$

Thus, these approaches are equivalent to the overrelaxed approach. Among the formulations shown above, the expression given by Eq. (12) is favored because the extension of the other expressions to three-dimensional flows is much more complicated. It is interesting to be aware of that a form similar to Eq. (12) has also been proposed by Mathur and Murthy [3].



### Mass Fluxes

The velocity at face $e$ shown in Figure 4 is calculated from

$$\overrightarrow{V}_e = \overline{\overrightarrow{V}}_e - (D_e \nabla p_e - D_e \overline{\nabla p}_e) \tag{19}$$

where

$$D_e = \left(\frac{\Delta v}{A_P^u}\right)_e = \frac{1}{2}\left[\left(\frac{\Delta v}{A_P^u}\right)_P + \left(\frac{\Delta v}{A_P^u}\right)_E\right] \tag{20}$$

In Eq. (19), the overbars denote the values interpolated from the two neighboring nodes $P$ and $E$. $A_P^u$ is the main coefficient of the difference momentum equation. The mass flux is then obtained by

$$\dot{m}_e = \rho_e \overrightarrow{V}_e \cdot \vec{s} = \overline{\rho}_e \overline{\overrightarrow{V}}_e \cdot \vec{s} - \overline{\rho}_e D_e (\nabla p_e \cdot \vec{s} - \overline{\nabla p}_e \cdot \vec{s}) \tag{21}$$

The difference of the two pressure forces in parentheses is approximated, by replacing $\vec{s}$ by $\vec{d}$, as

$$\nabla p_e \cdot \vec{s} - \overline{\nabla p}_e \cdot \vec{s} \approx \nabla p_e \cdot \vec{d} - \overline{\nabla p}_e \cdot \vec{d} \tag{22}$$

This approximation does not make the second-order accuracy of the expression (21) for $\dot{m}$ deteriorate because the difference between the two gradients simply represents a third-order correction to the velocity [15]. When the overrelaxed approach is employed, the mass flux becomes

$$\dot{m}_e = \overline{\rho}_e \overline{\overrightarrow{V}}_e \cdot \vec{s} - A_E^P [(p_E - p_P) - \overline{\nabla p}_e \cdot \vec{\delta}_{PE}] \tag{23}$$

where

$$A_E^p = \bar{\rho}_e D_e \frac{s^2}{\vec{\delta}_{PE} \cdot \vec{s}} \tag{24}$$

$A_E^p$ is the coefficient connecting point $P$ and point $E$ in the pressure-correction equation discussed later.

### Pressure Gradients

The pressure gradient is approximated, using the divergence theorem, in the following form:

$$\nabla p = \frac{1}{\Delta v} \int_{\Delta v} \nabla p \, dv = \frac{1}{\Delta v} \sum_{f=1}^{n} p_f \vec{s}_f \tag{25}$$

For a component of the gradient in the $x_i$ direction, it is given as

$$\frac{\partial p}{\partial x_i} = \frac{1}{\Delta v} \sum_{f=1}^{n} p_f (\vec{s}_f \cdot \vec{e}_i) \tag{26}$$

where $\vec{e}_i$ represents the unit vector in the $x_i$ direction and the face pressure $p_f$ is obtained using linear interpolation.

### Discretized Momentum Equation

By substituting the flux expressions (4) and (12) and the pressure gradient approximation (26) into Eq. (2), the following equation is obtained:

$$A_P \phi_P = \sum_{C=1}^{n} A_C \phi_C + S \tag{27}$$

where $\phi_C$ is the value at the neighboring cell node $C$ and $A_C$ is the coefficient connecting the nodes $P$ and $C$. The coefficient $A_C$ is made of the implicit parts of the convection and the diffusion fluxes. The source $S$ consists of the explicit parts of the fluxes and the volume integral of the pressure gradient.

### Pressure-Correction Equation

The pressure-correction equation can be derived from satisfaction of the continuity equation as follows. As suggested by Patankar [19], the velocity correction is related to the gradient of pressure correction in the following way:

$$\vec{V}_e' = \vec{V}_e^{**} - \vec{V}_e^{*} = -D_e \nabla p_e' \tag{28}$$

The mass flux is then calculated by

$$\begin{aligned}\dot{m}_e^{**} - \dot{m}_e^{*} &= -\overline{\rho}_e D_e \nabla p'_e \cdot \vec{s} \\ &= -\overline{\rho}_e D_e \nabla p'_e \cdot \vec{d} - \overline{\rho}_e D_e \overline{\nabla p'_e} \cdot (\vec{s} - \vec{d})\end{aligned} \tag{29}$$

When the overrelaxed approach is applied, it can be cast into the following form:

$$\dot{m}_e^{**} - \dot{m}_e^{*} = A_E^p (p'_P - p'_E) - \overline{\rho}_e D_e \overline{\nabla p'_e} \cdot (\vec{s} - \vec{d}) \tag{30}$$

where the coefficient $A_E^p$ is given in Eq. (24) and $D_e \overline{\nabla p'_e}$ is approximated by

$$D_e \overline{\nabla p'_e} = \frac{1}{2}(D_P \nabla p'_P + D_E \nabla p'_E) \tag{31}$$

By forcing the mass fluxes $m_f^{**}$ on all the faces surrounding the control volume considered to satisfy the mass conservation law, a pressure-correction equation is obtained.

$$A_p p'_p = \sum_{C=1}^{n} A_C p'_C + S_{p1} + S_{p2} \tag{32}$$

where the coefficient $A_C$ for a neighboring cell $E$ is just the $A_E^p$. The two sources are

$$S_{p1} = -\sum_{f=1}^{n} m_f^{*} \tag{33a}$$

$$S_{p2} = \sum_{f=1}^{n} \overline{\rho}_f D_f \overline{\nabla p'_f} \cdot (\vec{s} - \vec{d}) \tag{33b}$$

In $S_{p1}$ the mass flux $m_f^{*}$ is given in Eq. (23). The $S_{p2}$ term, representing the contribution of the cross-derivative of pressure, contains grid points other than the ones immediately neighboring the control volume considered. This term disappears in orthogonal meshes and is simply ignored by most researchers. However, this term gathers importance as the mesh becomes skew. It has been shown in the use of curvilinear grids that by including this cross-derivative term, a stable solution can be achieved even if the mesh is extremely skew [20–22]. In unstructured grid calculations, it is extremely difficult to treat this term implicitly, due to the inclusion of far neighboring grid points. To account for this term, a successive correction procedure is used [23].

First step:

$$A_P p_P^{(1)} = \sum_{C=1}^{n} A_C p_C^{(1)} + S_{p1} \tag{34}$$

Here only $S_{p1}$ is taken into consideration. After the first pressure correction $p^{(1)}$ is obtained, the old pressure $p$ is updated.

$$p^* = p + p^{(1)} \tag{35}$$

The velocity at each cell center and the mass flux at each cell face are also adjusted via

$$\vec{V}^{**} = \vec{V}^* - D\nabla p^{(1)} \tag{36a}$$

$$m_f^{**} = m_f^* + A_C^p(p_P^{(1)} - p_C^{(1)}) \tag{36b}$$

Second step:

$$A_P p_P^{(2)} = \sum_{C=1}^{n} A_C p_C^{(2)} + S_{p2}^{(1)} \tag{37}$$

where

$$S_{p2}^{(1)} = \sum_{f=1}^{n} \overline{\rho}_f D_f \overline{\nabla p_f^{(1)}} \cdot (\vec{s} - \vec{d}) \tag{38}$$

In this step the first pressure correction $p^{(1)}$ is used for calculating $S_{p2}$ and a second pressure correction $p^{(2)}$ is solved for. The pressure, velocity, and mass flux are further upgraded by

$$p^{**} = p^* + p^{(2)} \tag{39a}$$

$$\vec{V}^{***} = \vec{V}^{**} - D\nabla p^{(2)} \tag{39b}$$

$$\dot{m}_f^{***} = m_f^{**} - \overline{\rho}_f D_f \overline{\nabla p_f^{(2)}} \cdot (\vec{s} - \vec{d}) \tag{39c}$$

More corrections in the same manner as the second step can be undertaken.

### Solution Algorithm

The overall solution procedure can be described in the following sequence of steps.

1. Initial velocity and pressure fields are assumed.
2. The momentum equation (27) is solved to find the velocity.
3. The mass flux at cell face is computed from Eq. (23).
4. The first pressure correction is sought through solving the pressure-correction equation (34), and the pressure, velocity, and mass flux are updated accordingly.
5. Equation (37) is solved to find the second pressure correction, and the velocity and pressure fields are adjusted. More correction steps in the same way can be performed if it is necessary.

Steps 2–5 are repeated until convergence for the momentum and the pressure-correction equations is reached. It is noted that the convergence of pressure correction is based on the first pressure-correction step [Eq. (34)] because when the pressure correction approaches zero, mass conservation is ensured.

In order to take advantage of the sparse characteristic in solving the large system of algebraic equations raised from discretization, iterative methods are usually employed. In the past several decades the tridiagonal matrix algorithm (TDMA) and Stone's SIP have been the most popular. However, these algorithms are no longer applicable in the unstructured mesh system because the coefficient matrices are not banded. An effective algorithm suitable for unstructured grid calculation is the preconditioned conjugate gradient method. In this study the symmetric pressure-correction equation is solved by the incomplete Cholesky conjugate gradient method proposed by Kershaw [24], and the nonsymmetric transport equations by the biconjugate gradient method of Fletcher [25].



## RESULTS AND DISCUSSION

The following flow cases are tested to validate the above method: lid-driven cavity flows, diffuser flows, and the flow in a stirred tank. The first two cases are two-dimensional and the last serves as an example which extends the methodology to three-dimensional flow. Central differencing is adopted in the first two flow calculations, whereas the upstream-biased scheme is used in the stirred-tank flow, with $\gamma$ being setting at 0.9.

### Lid-Driven Cavity Flows

As shown in Figure 5*a*, a cavity is skew at an angle $\alpha$ with respect to the $y$ axis. The lid at the top of the cavity moves at a constant speed. Due to the transport of shear stress from the moving lid by the molecular viscosity a flow is set up in the cavity. Benchmark solutions have been obtained by Ghia et al. [26] for an orthogonal cavity ($\alpha = 0$) and by Demirdzic et al. [27] for skew cavities. To validate the current method these problems were solved using both quadrilateral and triangular meshes. For the orthogonal cavity the quadrilateral grid consists of $128 \times 128$ cells, which was adopted by Ghia et al. [26] as well. To generate the triangular mesh a $91 \times 91$ rectilinear grid was constructed first and then each quadrilateral was divided into two triangles. The calculated $u$ velocity along the vertical centerline and the $v$ velocity along the horizontal centerline for Reynolds numbers $\mathrm{Re} = 100$ and 1,000 are shown in Figure 6. It is apparent that the present predictions by both grids are in good agreement with the data of Ghia et al. for the low-Reynolds-number case. For the high-Reynolds-number flow the peaks of the velocity profiles are slightly underpredicted by using the triangular grid. For the flow in the skew cavity, the triangular grids are generated using PATRAN. The grids are made of about 14,000 triangular cells, which are equivalent to a $120 \times 120$ quadrilateral grid as adopted in the following calculations. The triangular grid for $\alpha = 60^\circ$ is sketched in Figure 5*b*. A portion of the grid layout is magnified and illustrated in the inset. It can be seen that the computational cells, different from those used in the orthogonal cavity flow, are much more nondistorted, i.e., close to equilateral triangles. As shown in Figure 7, the

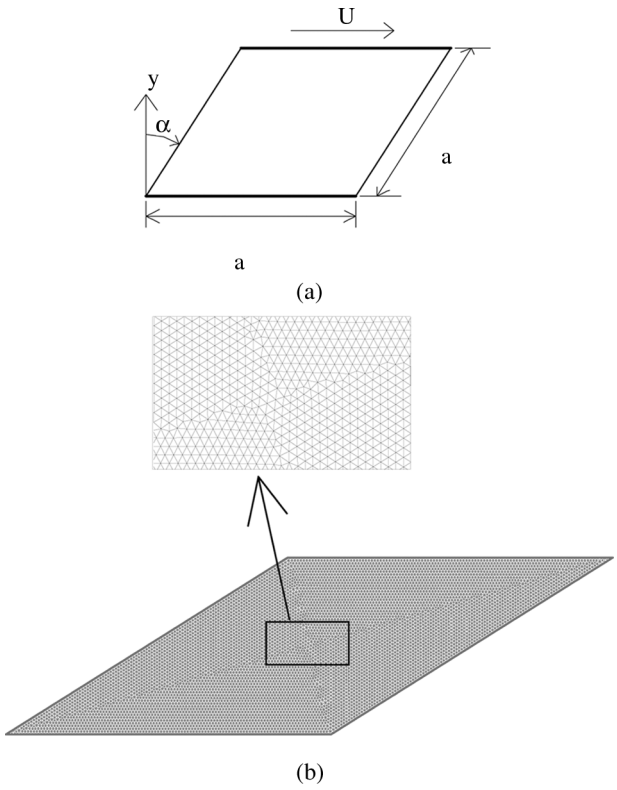


**Figure 5.** Illustration of (*a*) cavity flow configuration and (*b*) triangular grid layout for $\alpha = 60^\circ$ cavity.

predictions of $u$ and $v$ velocities along the centerlines by both grid systems do reproduce the data of Demirdzic et al. [27] well for $\alpha = 45^\circ$ and $60^\circ$. Also shown in the case of $\alpha = 60^\circ$ are the effects of grid size. When the grid density increases, the calculations approach the "exact" one. The predictions by the grid levels higher than $80 \times 80$ become grid independent.

In solving the pressure-correction equation a successive correction procedure has been introduced to deal with the cross-derivative term $S_{p2}$, which arises in skew meshes. The number of correction steps requires optimization such that an efficient and stable solution is obtained. In calculations the process of underrelaxation suggested by Patankar [19] was necessitated to assure convergence. For the case with $\alpha = 60^\circ$, Figure 8*a* presents the required number of iterations for convergence against the underrelaxation factor of velocity urf($u$) by setting the underrelaxation factor of pressure urf($p$) = 0.2. On the other hand, the required iterations versus urf($p$) is shown in Figure 8*b*, in which urf($u$) is fixed at 0.8. The convergence criterion is based on the total residuals for both the momentum and pressure-correction equations to be less than $10^{-4}$. The number of correction steps is denoted as $k$ in the figures. Obviously, by ignoring the cross-derivative term ($k = 1$), the underrelaxation factor required for convergence is restricted in a small range that is much smaller than 1. By having more than one correction, this range is enlarged.

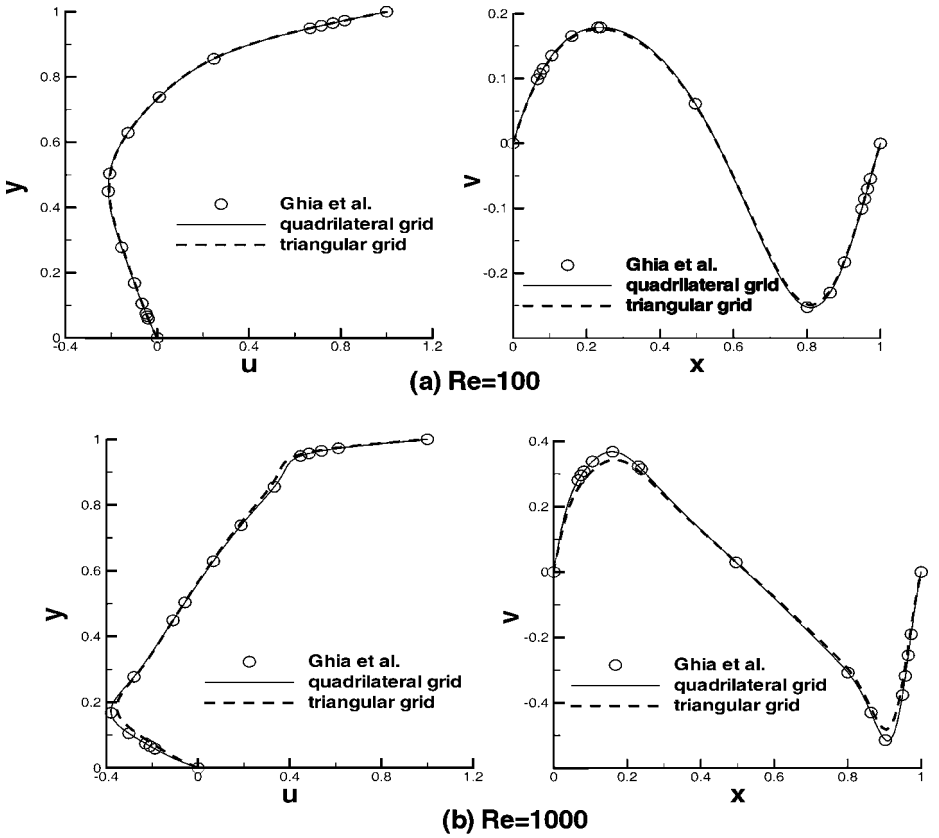


**Figure 6.** Comparison of velocities $u$ and $v$ along the vertical and horizontal centerlines in orthogonal cavity ($\alpha = 60°$): (*a*) Re = 100; (*b*) Re = 1,000.

Comparing with $k = 2$, further increase of $k$ to 3 does not help to increase the stability limits. A similar trend can also be observed in the other skew angles. It can also be noticed that minimum number of iterations for convergence is yielded for $k = 2$.

In the above calculations the overrelaxed approach was used for both the diffusion flux and the pressure-correction equation. In order to demonstrate the superiority of this approach the orthogonal-correction approach has also been tested. It was found that by using the orthogonal-correction approach it is difficult to obtain convergent solution when the skew angle becomes large enough.

## Diffuser Flows

A schematic drawing of the diffuser is shown in Figure 9. The expansion ratio of the diffuser $W2/W1$ is 3 and the height $S$ is equal to $W1$. The computational domain extends to $30S$ downstream of the diffuser entrance, which is much larger than the size of the recirculating flow formed in the diffuser. The inlet velocity was assumed to be fully developed and the zero gradient condition was imposed

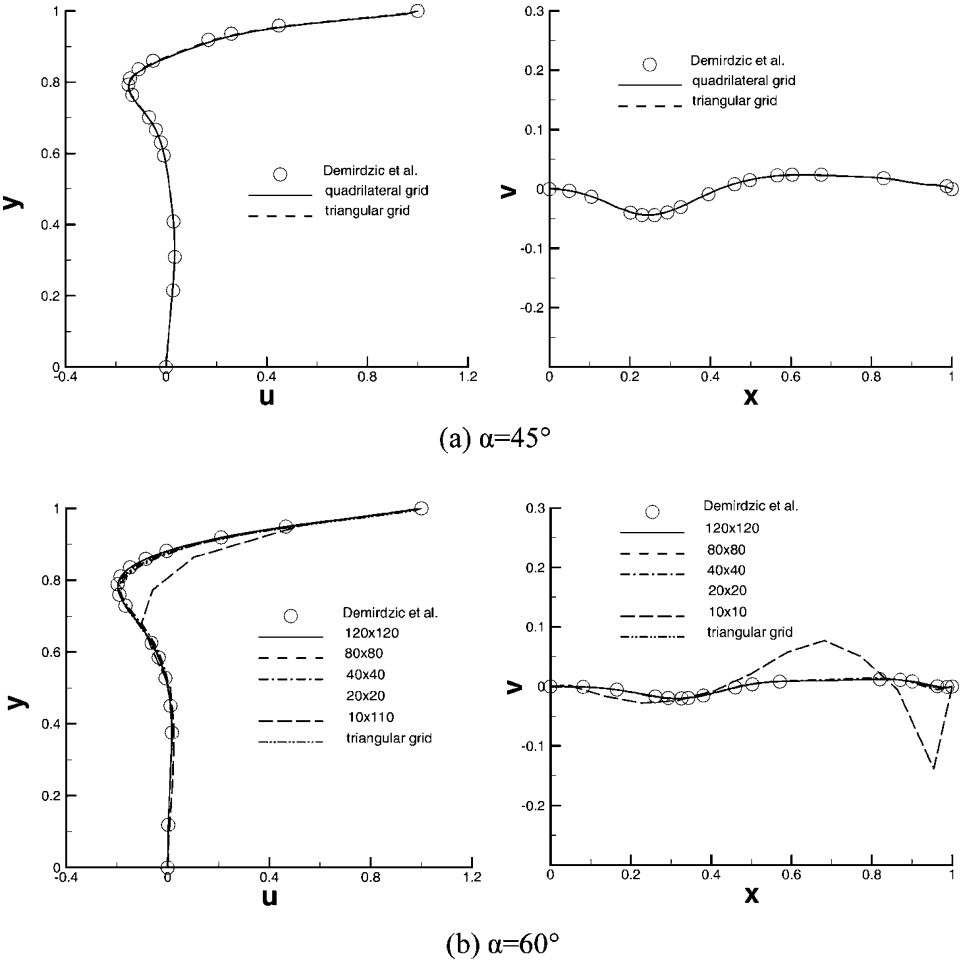


**Figure 7.** Comparison of velocities $u$ and $v$ along the vertical and horizontal centerlines for Re = 1,000 in skew cavity: (*a*) $\alpha = 45°$; (*b*) $\alpha = 60°$.

at the outlet. Two Reynolds numbers were considered: Re = 56 and 114. The definition of Reynolds number is based on $W1$ and the inlet centerline velocity.

Experimental data are available for the sudden expansion case (diffuser angle $\alpha = 90°$) [28]. The domain is divided into $100 \times 50$ rectangular cells. To create a triangular mesh, a $77 \times 33$ rectilinear grid was generated and each rectangle was then divided into two triangles. The comparison of predictions with measurements at a number of $x$ stations in Figure 10 shows good agreement for the low-Reynolds-number case, though a certain degree of difference exists. In calculations the overall mass flow rate at each cross section is assured to be identical when the solution converges. However, integrating the measured velocity profile indicates that the mass is not conserved. This causes the disagreement between predictions and measurements, especially at downstream locations. Similar conclusions could be found in the

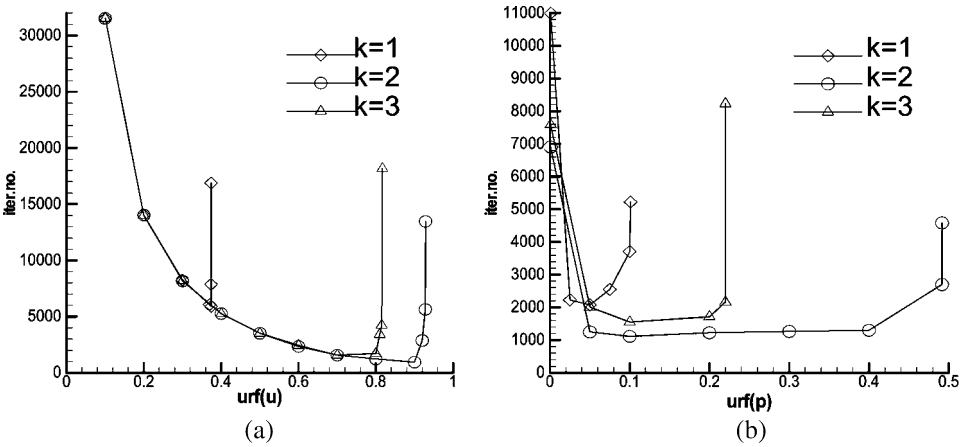


**Figure 8.** Number of iterations against (*a*) underrelaxation factor of velocity and (*b*) underrelaxation factor of pressure for 60° cavity flow.

previous study [29]. For the high Reynolds number the flow becomes asymmetric, with a large recirculating flow behind one backward step and a small recirculation zone behind the other step. The comparison with measurements indicates the degree of flow asymmetry being less significant in the predictions. The cause of this discrepancy can be attributed mainly to the fact that the flow in the experiments tends to become three-dimensional in the recirculation region, being supported by the photographs of Durst et al. [28].

The diffuser with $\alpha = 45°$ was used for testing the effects of number of pressure-correction steps. A grid with $80 \times 40$ quadrilaterals was employed. The sketch of streamlines seen in Figure 11 indicates that, similar to the sudden-expansion case, the flow pattern is symmetric for $\mathrm{Re} = 56$ and asymmetric for $\mathrm{Re} = 114$. For the latter a large recirculating flow forms on one side of the diffuser and a small one on the other side. Like the cavity flow, the underrelaxation factor urf($p$) shown in Figure 12*a* for $\mathrm{Re} = 114$ is greatly limited and much smaller than 1 when only one correction step is performed in each iteration cycle. By taking account of the $S_{p2}$ via adopting more corrections, the convergence range is greatly enlarged. Still, with $k = 2$ it brings about wider convergence range and fewer iterations. The above results are obtained by using the overrelaxed approach. The corresponding results

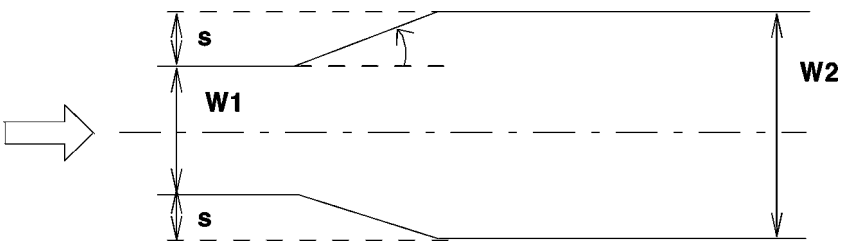


**Figure 9.** Diffuser flow configuration.

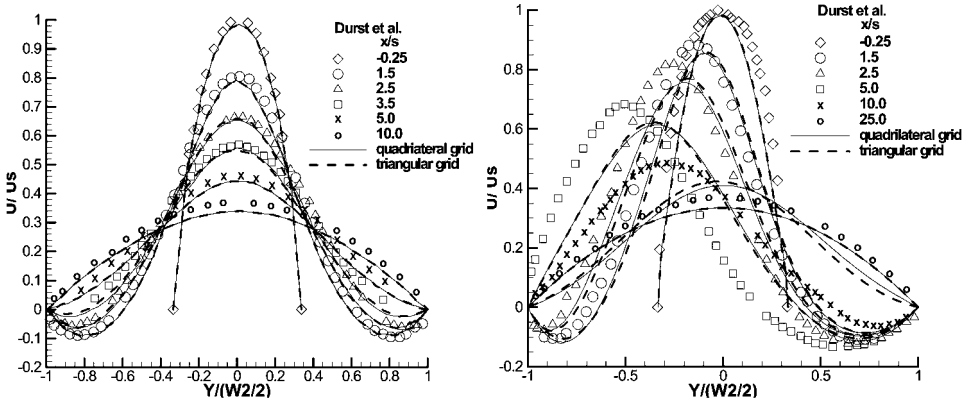


**Figure 10.** Comparison of axial velocities at a number of $x$ stations in sudden expansion diffuser: (*a*) Re = 56; (*b*) Re = 114.

for the orthogonal-correction approach are presented in Figure 12b. It can be seen that, compared with the overrelaxed approach, the convergence ranges for $k = 1$ and 3 by this approach are greatly narrowed.

## Flow in a Stirred Tank

Stirred-tank reactors are widely used in chemical industries. In this equipment the flow is driven by a rotating impeller. A schematic drawing of the agitation system considered in the present calculations is shown in Figure 13*a*. The impeller used for agitating the fluid consists of six blades with a pitch angle $\alpha = 45^\circ$. There are four baffles on the surrounding wall of the tank. The flow is inherently unsteady. Since transient calculations are very time-consuming, the flow is assumed to be quasi-steady in the modeling. It was shown [30] that with the steady-state approximation, good agreements with fully unsteady calculations can be achieved. In the steady-state

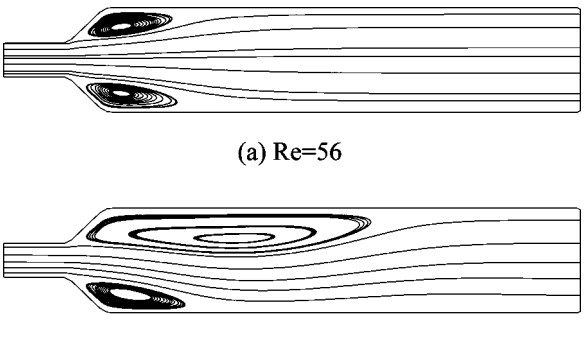


**Figure 11.** Flow streamlines in 45° diffuser: (*a*) Re = 56; (*b*) Re = 114.

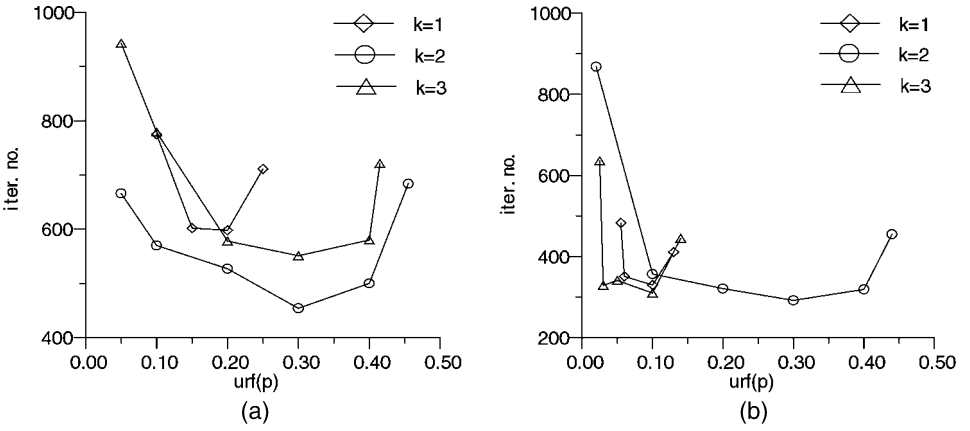


**Figure 12.** Number of iterations against underrelaxation factor of velocity for 45° diffuser at Re = 114: (*a*) overrelaxed approach; (*b*) orthogonal-correction approach.

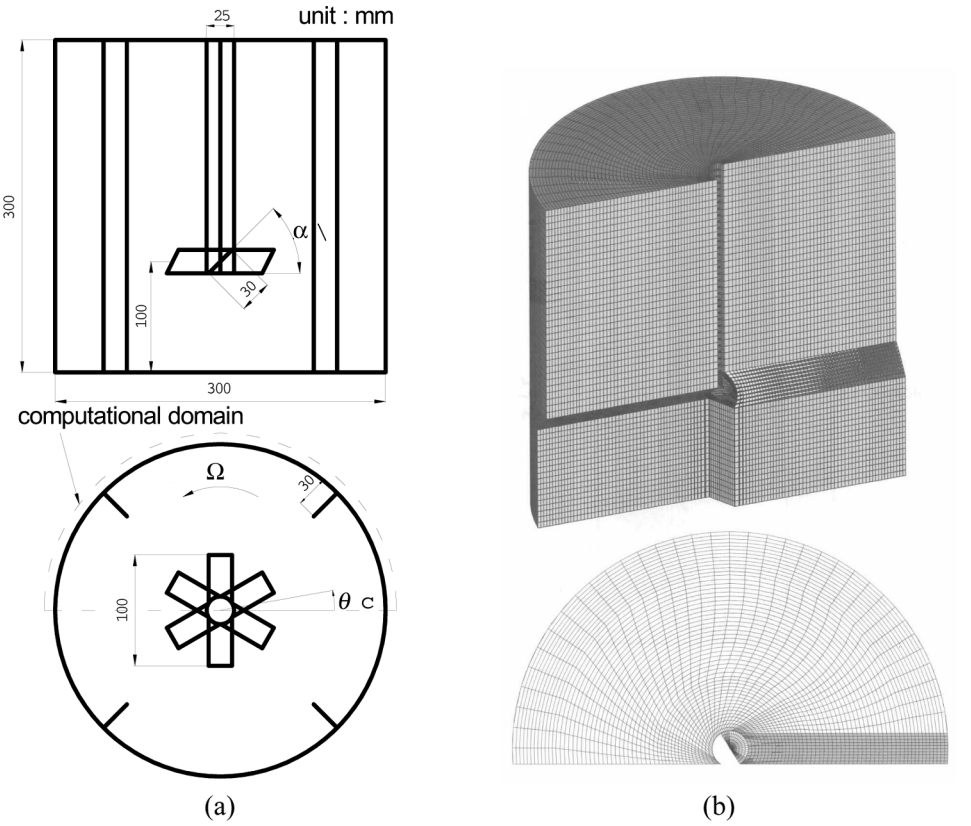


**Figure 13.** Illustration of (*a*) stirred-tank configuration and (*b*) grid layout.

approach the volume swept by the impeller, i.e., the passage region between blades, is situated on a rotating frame of reference, while a stationary frame is assigned to the rest of the tank. In the passage region, appropriate rotational body forces need to be included. At the interface of the two regions, a suitable transformation of the velocities from one reference frame to another is required.

Due to the symmetrical arrangement of the blades and the baffles, only half the tank is considered in calculations (see Figure 13*a*). Periodic conditions are imposed on the radial boundary planes. A layout of the computational grid is given in Figure 13*b*. To generate this grid, the domain was divided into 40 blocks first, and then an algebraic method was employed to construct the mesh in each block. The impeller rotates at 3.53 rev/s. At this speed the flow is inevitably turbulent. To account for turbulent effects the $k$–$\varepsilon$ model was used. To illustrate the flow structure, a plot of velocity vectors on a $\theta = 90^\circ$ plane is shown in Figure 14. The most prominent flow structure is a large circulation formed by a jet discharging from the bottom edge of the blade. The jet is caused mainly by the centrifugal force induced by the rotating impeller. The discharging angle is mostly dependent on the pitch angle of the blade. Another circulation is visible in the region near the axis below the impeller. The predictions are validated via comparison with measurements [31], as shown in



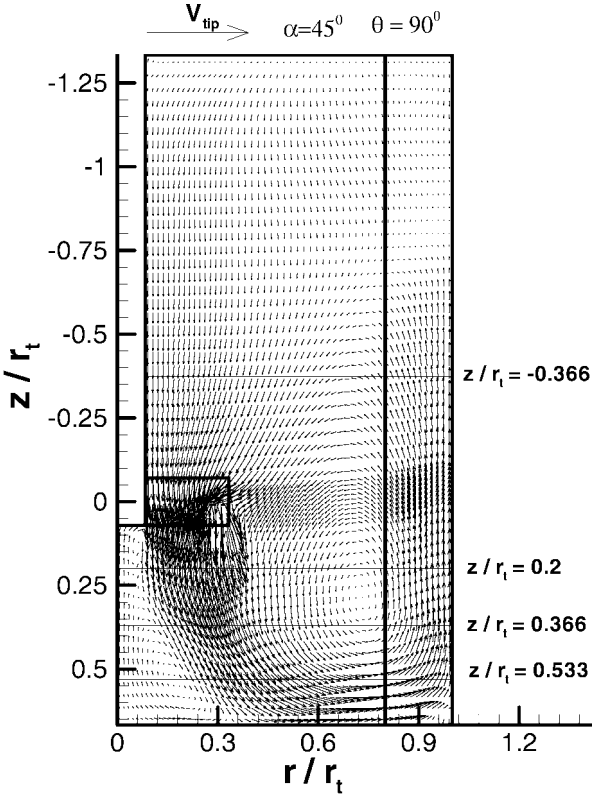


**Figure 14.** Velocity vectors on $\theta = 90^\circ$ plane.

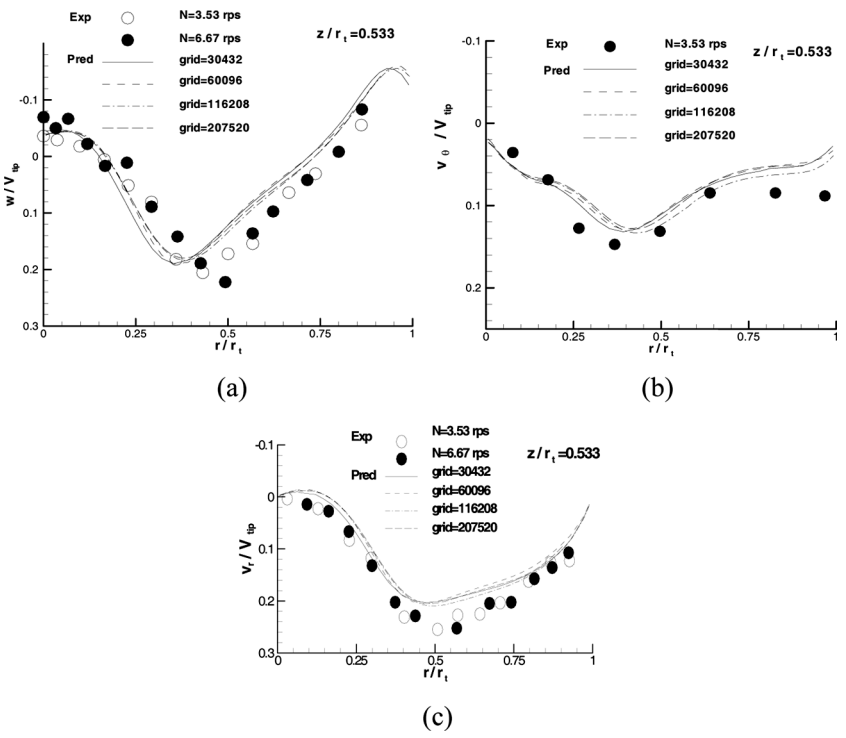


**Figure 15.** Comparison with measurements: (*a*) axial velocity; (*b*) tangential velocity; (*c*) radial velocity.

Figure 15. In this figure the radial variations of velocities in the axial, radial, and tangential directions at $z/r_t = 0.533$ (see Figure 14 for the location) for a number of grids ranging from 30,342 to 207,520 cells are presented. In the jet region all the velocity components increase with the radius, followed by a decay outside the jet. Although the velocity peaks of the jet are underpredicted, the flow trends are fully reflected in the calculations. The disagreement between the predictions and the measurements can be attributed mainly to the assumption of steady state and the deficiency of the turbulence model. In addition, it is time averaging, rather than ensemble averaging, carried out in the experiments. Therefore, the accuracy of the measurements is not without problem.

## CONCLUSIONS

A finite-volume algorithm is presented for solving incompressible flows. This algorithm is based on the pressure-correction concept and is suitable for unstructured grid calculation. It features the following characteristic.

1. The grid is arranged in a cell-centered, collocated manner.
2. The divergence theorem is applied and surface vectors are employed in calculation of fluxes and gradients. In this way the discretization is equally applicable to two- and three-dimensional problems.

3. Vector forms are used throughout the formulation of discretization. Therefore, the programming of the algorithm can easily be extended from two dimensions to three dimensions by simply including the additional component.
4. The overrelaxed approach is adopted for calculation of diffusion fluxes and in the formulation of the pressure-correction equation. This approach can be implemented directly into three-dimensional flows without requiring reformulation.
5. Successive corrections are used to deal with the cross-derivative term in the pressure-correction equation raised by the overrelaxed approach. Testing indicates that two correction steps are the most preferred.



## REFERENCES

1. M. Williams, The Solution of the Two-Dimensional Incompressible Flow Equations on Unstructured Triangular Meshes, *Numer. Heat Transfer B*, vol. 23, pp. 309–325, 1993.
2. L. Davidson, A Pressure Correction Method for Unstructured Meshes with Arbitrary Control Volumes, *Int. J. Numer. Meth. Fluids*, vol. 22, pp. 265–281, 1996.
3. S. R. Mathur and J. Y. Murthy, A Pressure-Based Method for Unstructured Meshes, *Numer. Heat Transfer B*, vol. 31, pp. 195–215, 1997.
4. Y. G. Lai, An Unstructured Grid Method for a Pressure-Based Flow and Heat Transfer Solver, *Numer. Heat Transfer B*, vol. 32, pp. 267–281, 1997.
5. Y. G. Lai, Unstructured Grid Arbitrarily Shaped Element Method for Fluid Flow Simulation, *AIAA J.*, vol. 38, pp. 2246–2252, 2000.
6. D. Kim and H. Choi, A Second-Order Time-Accurate Finite Volume Method for Unsteady Incompressible Flow on Hybrid Unstructured Grids, *J. Comput. Phys.*, vol. 162, pp. 411–428, 2000.
7. Y.-H. Hwang, Calculation of Incompressible Flow on a Staggered Triangular Grid, Part I: Mathematical Formulation, *Numer. Heat Transfer B*, vol. 27, pp. 323–336, 1995.
8. S. Rida, F. McKenty, F. L. Meng, and M. Reggio, A Staggered Control Volume Scheme for Unstructured Triangular Grids, *Int. J. Numer. Methods Fluids*, vol. 25, pp. 697–717, 1997.
9. M. Thomadakis and M. Leschziner, A Pressure-Correction Method for the Solution of Incompressible Viscous Flows on Unstructured Grids, *Int. J. Numer. Methods Fluids*, vol. 22, pp. 581–601, 1996.
10. G. K. Despotis and S. Tsangaris, Fractional Step Method for Solution of Incompressible Navier-Stokes Equations on Unstructured Triangular Meshes, *Int. J. Numer. Meth. Fluids*, vol. 20, pp. 1273–1288, 1996.
11. R. A. Nicolaides, Flow Discretization by Complementary Volume Techniques, AIAA Paper 89-1978, 1989.
12. B. Niceno and E. Nobile, Numerical Analysis of Fluid Flow and Heat Transfer in Periodic Wavy Channels, *Int. J. Heat Fluid Flow*, vol. 22, pp. 156–167, 2001.
13. J. C. Cavendish, C. A. Hall, and T. A. Porsching, A Complementary Volume Approach for Modelling Three-Dimensional Navier-Stokes Equations Using Dual Delaunay/Voronoi Tessellations, *Int. J. Numer. Meth. Heat Fluid*, vol. 4, pp. 329–345, 1994.
14. C. M. Rhie and W. L. Chow, Numerical Study of the Turbulent Flow Past an Airfoil with Trailing Edge Separation, *AIAA J.*, vol. 21, pp. 1525–1532, 1983.
15. F. S. Lien and M. A. Leschziner, A General Non-orthogonal Collocated Finite Volume Algorithm for Turbulent Flow at All Speeds Incorporating Second-Moment Turbulence-Transport Closure, Part 1: Computational Implementation, *Comput. Meth. Appl. Mech. Eng.*, vol. 114, pp. 123–148, 1994.

16. B. P. Leonard, A Stable and Accurate Convection Modeling Procedure Based on Quadratic Upstream Interpolation, *Comput. Meth. Appl. Mech. Eng.*, vol. 19, pp. 59–98, 1978.
17. Y.-Y. Tsui, A Study of Upstream-Weighted High-Order Differencing for Approximation to Flow Convection, *Int. J. Numer. Meth. Fluids*, vol. 13, pp. 167–199, 1991.
18. H. Jasak, Error Analysis and Estimation for the Finite Volume Method with Applications to Fluid Flows, Ph.D. thesis, Imperial College, University of London, London, UK, 1996.
19. S. V. Patankar, *Numerical Heat Transfer and Fluid Flow*, McGraw-Hill, New York, 1980.
20. M. Peric, Analysis of Pressure-Velocity Coupling on Nonorthogonal Grids, *Numer. Heat Transfer B*, vol. 17, pp. 63–82, 1990.
21. Y.-Y. Tsui and P.-W. Wu, Investigation of the Mixing Flow Structure in Multilobe Mixers, *AIAA J.*, vol. 34, 1386–1391, 1996.
22. Y.-Y. Tsui, S.-W. Leu, C.-C. Lin, and P.-W. Wu, Heat Transfer Enhancement by Multi-lobe Vortex Generators: Effects of Lobe Parameters, *Numer. Heat Transfer A*, vol. 37, pp. 653–672, 2000.
23. J. H. Ferziger and M. Peric, *Computational Methods for Fluid Dynamics*, Springer-Verlag, Berlin, 1997.
24. D. S. Kershaw, The Incomplete Cholesky Conjugate Gradient Method for the Iterative Solution of Systems of Linear Equations, *J. Comput. Phys.*, vol. 26, pp. 43–65, 1978.
25. R. Fletcher, Conjugate Gradient Methods for Indefinite Systems, *Lecture Notes Math.*, vol. 506, pp. 774–789, 1976.
26. U. Ghia, K. N. Ghia, and C. T. Shin, High-Re Solutions for Incompressible Flow Using the Navier–Stokes Equations and a Multigrid Method, *J. Comput. Phys.*, vol. 48, pp. 387–411, 1982.
27. I. Demirdzic, Z. Lilek, and M. Peric, Fluid Flow and Heat Transfer Test Problems for Non-orthogonal Grids: Bench-Mark Solutions, *Int. J. Numer. Meth. Fluids*, vol. 15, pp. 329–354, 1992.
28. F. Durst, A. Melling, and J. H. Whitelaw, Low Reynolds Number Flow over a Plane Symmetric Sudden Expansion, *J. Fluid Mech.*, vol. 64, part 1, pp. 111–128, 1974.
29. Y.-Y. Tsui and C.-K. Wang, Calculation of Laminar Separated Flow in Symmetric Two-dimensional Diffusers, *ASME J. Fluids Eng.*, vol. 117, pp. 612–616, 1995.
30. K. Wechsler, M. Breuer, and F. Durst, Steady and Unsteady Computations of Turbulent Flows Induced by a 4/45° Pitched-Blade Impeller, *ASME J. Fluids Eng.*, vol. 121, pp. 318–329, 1999.
31. V. V. Ranade and J. B. Joshi, Flow Generated by Pitched Blade Turbines I: Measurements Using Laser Doppler Anemometer, *Chem. Eng. Commun.*, vol. 81, pp. 197–224, 1989.